OMICS Journal of Radiology
ISSN: 2167-7964

Li, OMICS J Radiology 2013, 2:6
DOI: 10.4172/2167-7964.1000137

Review Article Open Access

Dual-Energy CT with Fast-kVp Switching and Its Applications in Orthopedics

Baojun Li*

Department of Radiology, Boston University School of Medicine, USA

Abstract

The metal artifacts obscure or mimic pathologies and thus severely limit the diagnostic value of CT imaging in orthopedic applications. The fundamental root cause is the beam hardening effect due to the polychromatic X-ray beam. Recently, dual-energy CT with fast-kVp switching technique has been introduced that allows synthetic monochromatic energy images to be generated through material decomposition. These monochromatic energy images are not only free of metal artifacts, but also available at a broad energy range for optimal contrast at bone-tissue interface. This article summarizes the principle of this advanced CT technology with emphasis in its capability in suppressing metal implant-induced CT artifacts.

Keywords: CT; Metal artifacts; Dual energy; Fast-kVp switching

Introduction

Dual-energy CT is an imaging technique that has been known and extensively studied for many decades [1-8]. However, due to various technical challenges, only recently has dual-energy CT imaging become a reality. Recent advances in CT scanner technologies have generated a renewed interest in dual-energy CT [9-14], which has led to the commercialization of dual-energy CT systems available for routine clinical use [10,12-14].

Dual-energy CT is a special CT imaging procedure in which two CT scans of a patient are acquired in different X-ray tube potentials (and spectra) and used to perform energy- and material-selective reconstruction of the patient. Relative to conventional single-energy CT imaging, dual-energy CT imaging offers the capability to enhance material differentiation and reduce beam hardening effect.

Conventional dual-energy CT exam is accomplished by so-called "rotate-rotate" technique: A low-kVp CT exam is acquired, and then the patient is translated back to the origin, followed by the acquisition of a high-kVp CT exam. Similar to Digital Subtraction Angiograph (DSA), this technique is very sensitive to patient motion because the time interval between the two kVps is in the order of seconds. As a result, poor spatial-temporal registration between high- and low-kVp X-ray beams is a major source of image artifacts in conventional dual-energy CT imaging. Compared to single-energy CT, motion-induced artifacts, such as blurring of the edges and streaks centered on objects that are moving are more severe in dual-energy CT. Furthermore, patient motion can be falsely interpreted as a change in tissue composition, which, typically manifested as light-and-dark edge effect around the moving objects, can cause inaccurate material densities and/or mis-diagnosis (Figure 1).

To address the motion issue, a fast-kVp switching (FKS) dual-energy CT imaging method, where kVp is rapidly switched between low- and high-kVp in adjacent views, has recently been proposed [12-14]. Compared to conventional dual-energy CT imaging, FKS dual-energy CT imaging has several benefits including fine temporal view registration, helical and axial acquisitions, and full field of view. It also presents several design challenges that warrant careful considerations.

Image Acquisition

X-ray tube/generator

The fundamental solution to avoid the motion issue is to acquire the low- and high-kVp projections on a view-by-view basis in a single gantry rotation. This enables precise spatial-temporal registration of two different kVps, thus freezing motion and significantly reducing artifact.

The X-ray generation system must enable the rapid kVp switching to achieve sufficient energy separation and view sampling speed. The generator and tube must be capable of reliably switching between 80 and 140 kVp, and have the capability to support sampling rate as quickly as every 150 micro-seconds. To ensure the signal fidelity, X-ray generator with ultra-low impedance of tens of micro-seconds is also necessary.

Following the acquisition, correction calibrations are applied to the

Figure 1: Patient motion is a major source of image artifacts in conventional dual-energy CT imaging due to poor spatial-temporal registration of high- and low-kVp x-ray beams. Dual-energy CT is in general more sensitive to patient motion than single-energy CT because material decomposition requires the two rays to pass through the same anatomy. In this example, artifacts manifested as light-and-dark edge effect near intestinal boundaries can be falsely interpreted as a change in tissue composition. Image courtesy of Robert Beckett, GE Healthcare, Waukesha, WI.

***Corresponding author:** Baojun Li, Department of Radiology, Boston University School of Medicine, USA, E-mail: baojunli@bu.edu

Received June 20, 2013; **Accepted** July 22, 2013; **Published** August 01, 2013

Citation: Li B (2013) Dual-Energy CT with Fast-kVp Switching and Its Applications in Orthopedics. OMICS J Radiology 2: 137 doi:10.4172/2167-7964.1000137

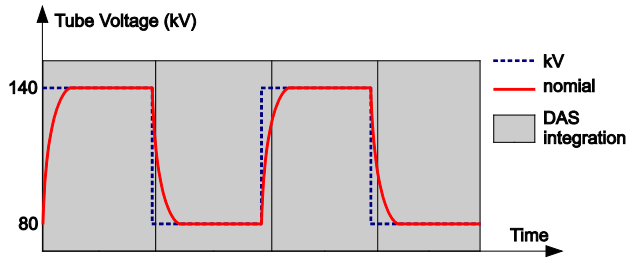

Figure 2: The rise and fall of actual kVp form complicates the spectral calibration of FKS dual-energy CT.

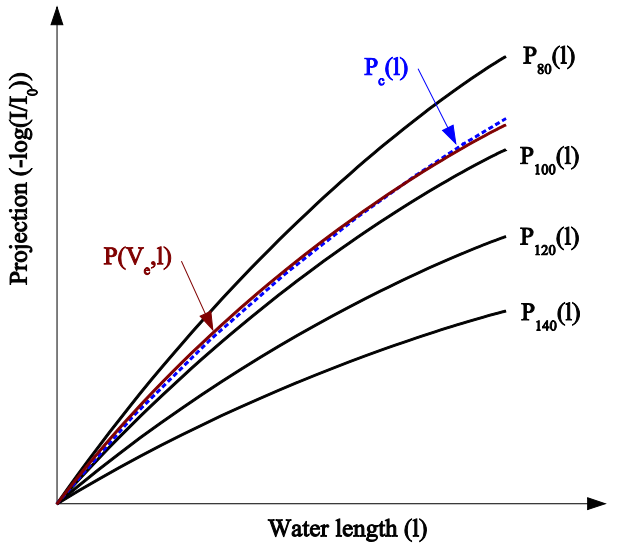

Figure 3: The estimation of effective spectrum in FKS dual-energy CT imaging. Pc(l) represents the equivalent X-ray attenuation of the estimated spectrum by Equation 4. P(Ve,l) is the measured X-ray attenuation of the fast-kVp system. It is obvious that the estimated spectrum Pc(l) matches the actual spectrum P(Ve,l) with minimal difference. Image courtesy of Dr Dan Xu of GE Global Research, Schenectady, NY.

data. The rise and fall of the kVp waveform complicates the spectral calibration. Figure 2 illustrates the actual kVp waveform employed in FKS dual-energy acquisition. The non-ideal kVp rise/fall makes it difficult to find a fixed kVp that matches the same spectral response as the fast-kVp switching.

To estimate the effective energy, the unknown spectra of the low- and high-kVp are estimated as the weighted linear combination of single kVp spectra [15]. The unknown X-ray spectra of the low and high kVp views are estimated as the weighted sum of several known single kVp spectra:

$$S_p(E)=\sum_k^{N_k}\alpha_k S_k(E) \quad (1)$$

where $S_k(E)$ are the basis spectra of the single kVps, N_k is the total number of the basis spectra, and αk are the weights of the basis spectra. The self-normalized detector response to this spectrum can be written as:

$$R(d)=\frac{\int_E \sum_k \alpha_k S_k(E)E[1-e^{-\mu_d(E)t_d}]e^{-\sum_b \mu_b(E,d)I_b(d)}dE}{\sum_d \int_E \sum_k \alpha_k S_k(E)E[1-e^{-\mu_d(E)t_d}]e^{-\sum_b \mu_b(E,d)I_b(d)}dE} \quad (2)$$

in which, $\mu_d(E)$ is the linear attenuation coefficient of the detectors, t_d is detector thickness, $\mu_b(E,d)$ and $I_b(d)$ are respectively the linear attenuation coefficient and the thickness of bowtie material b corresponding to detector channel d. If one denotes

$$G_k(d)=\int_E S_k(E)E[1-e^{-\mu_d(E)t_d}]e^{-\sum_b \mu_b(E,d)I_b(d)}dE \quad (3)$$

Equation 2 can be simplified to

$$R(d)=\frac{\sum_k \alpha_k G_k(d)}{\sum_d \sum_k \alpha_k G_k(d)} \quad (4)$$

$R(d)$ can be measured through a fast switching air scan, and $G_k(d)$ can be calculated based on the system geometry. Hereby the weighting coefficients α_k can be solved from Equation 4 by least square fitting. The overall spectrum is decomposed into a superposition of several basis spectra through the measurement of the detector response to the bowtie attenuation.

The above spectrum estimation technique is graphically demonstrated in Figure 3. $P_c(I)$ epresents the equivalent X-ray attenuation of the estimated spectrum by Equation 4. $P(V_e,I)$ is the measured X-ray attenuation of the fast-kVp system. It is obvious that the estimated spectrum $P_c(I)$ matches the actual spectrum $P(V_e,I)$ with minimal difference.

Detector

The detector is a key contributor to fast-kVp switching acquisitions through its scintillator and data acquisition system. Detector primary decay and afterglow performance are critical to avoiding spectral blurring between views. Primary speed and afterglow refer to the decays of light emitting from the scintillator for several to tens of milliseconds after the X-ray source is switched off. This phenomenon is analogous to the decay of light signal on the television screen after it is turned off. The residual signal from one view smears information contained in the next during a scan, thereby causing degradation of spatial resolution and undesirable cross-contamination of spectra.

Gemstone scintillator material (GE Healthcare, Waukesha, WI) is a complex rare earth based oxide, which has a chemically replicated garnet crystal structure. This lends itself to imaging that requires high light output, fast primary speed, very low afterglow. Gemstone has a primary speed of only 30 ns, or 100 times faster than GOS (Gd_2O_2S), while also having afterglow that is only 20% of GOS, making it ideal for fast sampling [16]. The capabilities of the scintillator are also paired with an ultrafast data acquisition system (up to 7 enabling simultaneous acquisition of low- and high-kVp data at customary rotation speeds.

Flux

Compared to single-energy CT, the traditional flux issues are more challenging in FKS dual-energy CT imaging. There hereby needs to be a strategy for balancing the flux between the two spectra and a need for noise reduction processing (which will be discussed later in Section 4).

In dual-energy imaging, the flux ratio between the low- and high-kVps is in general constrained in such a way that the Contrast-to-Noise Ratio (CNR) is maximized. Multiple studies [17-19] have suggested the CNR is maximized with ~30% flux allocation, defined as the percentage of entrance skin exposure of the low-kVp to that of the low- and high-kVp combined. That is, roughly speaking, the exposure ratio between the low- and high-kVp is

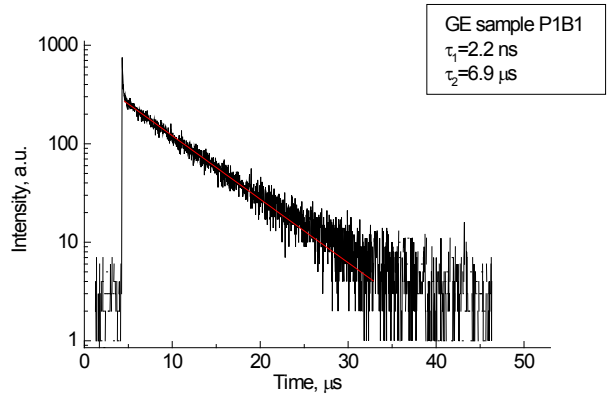

Figure 4: Gemstone scintillator material (GE Healthcare, Waukesha, WI) has a primary speed of only 30 ns, or 100 times faster than GOS (Gd2O2S), while also having afterglow that is only 20% of GOS, making it ideal for fast sampling. Image courtesy of Dr Haochuan Jiang, GE Healthcare, Waukesha, WI.

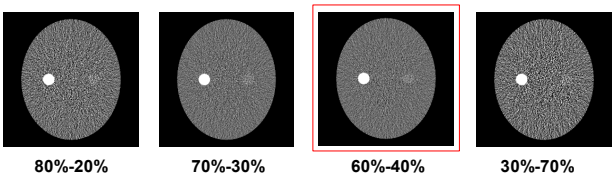

Figure 5: The reconstructed images of a simulated low contrast lesion (2 cm in diameter) embedded in an oval phantom. The simulations were conducted under identical conditions except for the view time ratio. The view time ratio is defined as the percentage of low-kVp view to high-kVp view in each low-high kVp pair. Comparing the results, 60%-40% view time ratio clearly offers the best CNR for the lesion detection. The result demonstrates the importance of balancing flux through modulating the view time in FKS dual-energy CT imaging.

$$\frac{N_L}{N_H} = \frac{1}{2} \quad . \tag{5}$$

The X-ray exposure is a function of X-ray energy spectrum, beam filtration, geometry, and the tube-current-time product (mAs). The FKS dual-energy CT system employs identical geometry and beam filtration for the 140 and 80 kVp acquisitions, which leaves only mAs adjustable. For the X-ray tubes used in CT, the X-ray exposure of a 140 kVp beam is roughly three-fold of that of an 80 kVp beam [20]. Therefore, according to Equation 5, the mAs ratio between low- and high-kVp views should be kept around 3/2. Based on above analysis, the view time ratio between the low- and high-kVp views should be 60%-40%. Figure 5 demonstrates the importance of balancing flux through modulating the view time in FKS dual-energy CT imaging. A simulated low contrast lesion (2 cm in diameter) is embedded in an oval phantom to show the impact of various view time ratios on the image quality. Comparing the results, 60%-40% view time ratio clearly offers the best CNR for the lesion detection.

Dose

FKS dual-energy CT has been designed to minimize the additional dose relative to single energy. In a recent dose and low contrast detectability (LCD) comparison [13,14], the effectiveness of this sampling scheme with respect to dose was demonstrated by matching the LCD at a slice thickness equal to 5 mm and object size of 3 mm. The LCD is a clinical-relevant image quality metric that quantifies image noise performance, making it ideal as an image quality target when measuring dose. The lower the LCD is, the less contrast a lesion of certain size (in mm) must have in order to be detected at a given confidence level (usually 95%).

Figure 6 compares the measured $CTDI_{vol}$ (in mGy) between a FKS dual-energy and routine (i.e., single-energy) abdominal CT exams as a function of monochromatic energy (in keV, dual-energy only) and tube current (in mA, single-energy only). The Single-Energy (SE) measurements are denoted as "SE xxx mA", where "xxx" describes the tube current, while the dual-energy measurements are denoted as "Mono xx keV", where "xx" represents the monochromatic energy (monochromatic energy will be discussed later in Section 2.3.2). All other acquisition protocols were the same between the two systems compared: kVp=120 kVp, gantry rotate speed=1.0s, bowtie=large body, slice thickness=5 mm, display field of view=22.5 cm).

From Figure 6, one can see that, with a tube current of 360 mA, the single-energy abdominal CT exam yields a LCD of 0.426% and a $CTDI_{vol}$ of 29.18 mGy for a 3 mm object. The FKS dual-energy abdominal CT exam (65 keV) produces a nearly identical LCD of 0.422% (0.01% = 0.1 HU) with a CTDIvol of 33.43 mGy for the same object size, or just 14% higher than that of a routine single-energy abdominal CT exam. These results were obtained using the uniform section of Catphan 600 phantom, which represents a patient with ~20 cm water-equivalent diameter.

Image Reconstruction

Projection-space material decomposition

The mass attenuation coefficient across the X-ray spectrum is a function of two independent variables: photoelectric effect and Compton scatter [1]. Based on this principle, the low- and high-kVp

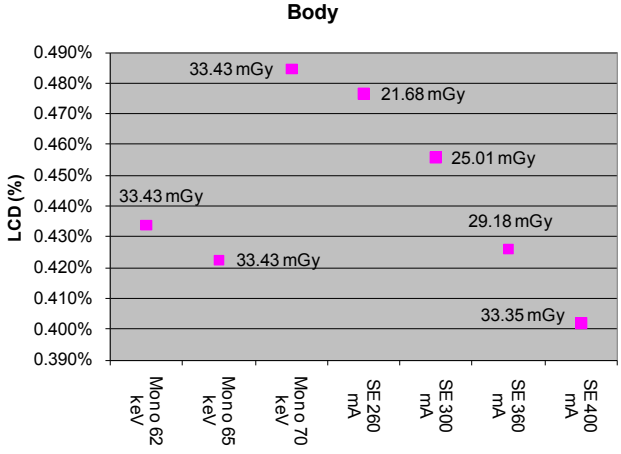

Figure 6: Comparison of the measured CTDIvol (in mGy) between a FKS dual-energy and routine (i.e., single-energy) abdominal CT exams as a function of monochromatic energy (in keV, dual-energy only) and tube current (in mA, single-energy only) (All other acquisition protocols were the same between the two systems compared: kVp=120 kVp, gantry rotate speed=1.0 s, bowtie=large body, slice thickness=5 mm, display field of view=22.5 cm). The single-energy (SE) measurements are denoted as "SE xxx mA", where "xxx" describes the tube current, while the dual-energy measurements are denoted as "Mono xx keV", where "xx" represents the monochromatic energy (monochromatic energy will be discussed later in Section 3.3). Image adapted from Li et. al, Med. Phys. 38(5), 2595-2601 (2011).

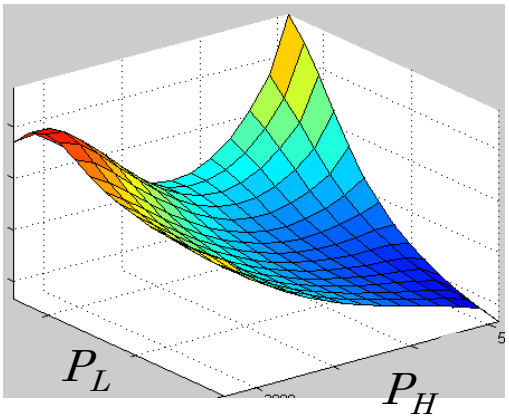

Figure 7: Equation 6 is over-determined and the resolution for polynomial coefficients α, β, χ, δ, ε, etc. can be found easily through least square fitting defined by Equation 7. The vertical axis represents the thickness of water.

projection data can be retrospectively transformed into a pair of basis materials (such as water and iodine).

Through a mathematical change of basis one can express the energy dependent attenuation observed in two kVp measurements in terms of two basis materials [14]:

$$\begin{aligned} f_1(\vec{l}) &= \alpha_1 p_H(\vec{l}) + \beta_1 p_L(\vec{l}) + \chi_1 p_H^2(\vec{l}) + \delta_1 p_L^2(\vec{l}) + \varepsilon_1 p_H(\vec{l}) p_L(\vec{l}) + \ldots\ldots \\ f_2(\vec{l}) &= \alpha_2 p_H(\vec{l}) + \beta_2 p_L(\vec{l}) + \chi_2 p_H^2(\vec{l}) + \delta_2 p_L^2(\vec{l}) + \varepsilon_2 p_H(\vec{l}) p_L(\vec{l}) + \ldots\ldots \end{aligned}, \quad (6)$$

where $\vec{l}$ is an arbitrary ray path, $P_H(\vec{l})$ and $P_L(\vec{l})$ denote the high- and low-kVp projection data, $f_i(\vec{l})$ represents the density of the basis material *i*, *α*, *β*, *χ*, *δ*, *ε* are polynomial coefficients, and the subscript H and L refer to the high and low kVp, respectively.

There are a couple of important facts in Equation 6 that should be noted here. First of all, $P_H(\vec{l})$ and $P_L(\vec{l})$ must be measured along the same ray path $\vec{l}$. This can be easily satisfied by FKS dual-energy CT imaging. The fast-kVp switching mechanism ensures the low- and high-kVp projection data are spatially and temporally co-registered (Note: Strictly speaking, the low- and high-kVp views incur a small angular offset relative to each other. To obtain truly co-registered projection pair, these views are interpolated to the same angular positions prior to material decomposition).

Secondly, the high-order terms in Equation 6 are critically important to account for spectral variation over the field of view due to source spectrum, bowtie filter, detector performance, and multi-material beam hardening effects [1]. As a consequence, projection-space material decomposition provides the opportunity for more quantitative precision than may be achieved with single-energy imaging. This is the key difference between FKS dual-energy CT imaging and image-space dual-energy CT imaging, which usually require additional beam hardening correction to recover the spectral information [21,22].

To solve Equation 6, dual-energy projection data corresponding to different thicknesses of water and iodine are acquired. Since modern CT scanners contain a large number of detector elements, Equation 6 is over-determined and the resolution for polynomial coefficients *α*, *β*, *χ*, *δ*, ε, etc. can be found easily through least square fitting:

$$\begin{aligned} &\arg\min \sum_{\vec{l}} \left\| f_1(\vec{l}) - \alpha_1 p_H(\vec{l}) - \beta_1 p_L(\vec{l}) - \chi_1 p_H^2(\vec{l}) - \delta_1 p_L^2(\vec{l}) - \varepsilon_1 p_H(\vec{l}) p_L(\vec{l}) - \ldots\ldots \right\|^2 \\ &\arg\min \sum_{\vec{l}} \left\| f_2(\vec{l}) - \alpha_2 p_H(\vec{l}) - \beta_2 p_L(\vec{l}) - \chi_2 p_H^2(\vec{l}) - \delta_2 p_L^2(\vec{l}) - \varepsilon_2 p_H(\vec{l}) p_L(\vec{l}) - \ldots\ldots \right\|^2 \end{aligned}. \quad (7)$$

Image reconstruction

Through material decomposition, the energy dependent attenuation measurements contained in kVp projections are transformed into energy independent basis material projection data corresponding to the two basis material pair (e.g., water and iodine).

Although the pair of basis material projection data (sinogram) essentially contains all useful information about the material being imaged, they are difficult to understand and interpreted by clinicians. A more useful form, which clinicians are familiar with, is the reconstructed images.

Having the identical geometry, the same reconstruction algorithm to reconstruct the single-energy CT images can therefore be applied to the first basis material projection data to obtain the corresponding basis material density image. The step is repeated for the second basis material as well.

An example is shown in Figure 8. Basis material density images represent the effective density for the anatomies necessary to create the observed low- and high-kVp attenuation measurements. For instance, pure water appears as 1,000 mg/cc in a water density image, 50 mg/cc of diluted iodine is labeled as such in an iodine density image, etc. Any non-basis material is mapped to both basis materials. For this reason, basis material density images are sometimes called "material density map".

Monochromatic energy image

Given the material basis density images, one can compute attenuation data that would be measured with a mono-energetic X-ray source by combining the material density images to create a monochromatic image at any specific energy level (in keV), *E* [14]:

$$\int u(\vec{l}, E) dl = \left(\frac{\mu_1}{\rho_1}\right)(E) \int f_1(\vec{l}) dl + \left(\frac{\mu_2}{\rho_2}\right)(E) \int f_2(\vec{l}) dl \,, \quad (8)$$

where (μ_i/ρ_i) represents the mass attenuation coefficient for material *i*. For consistency with the Hounsfield Unit, one can normalize the attenuation measurement with respect to water. A clinical example is shown in Figure 9.

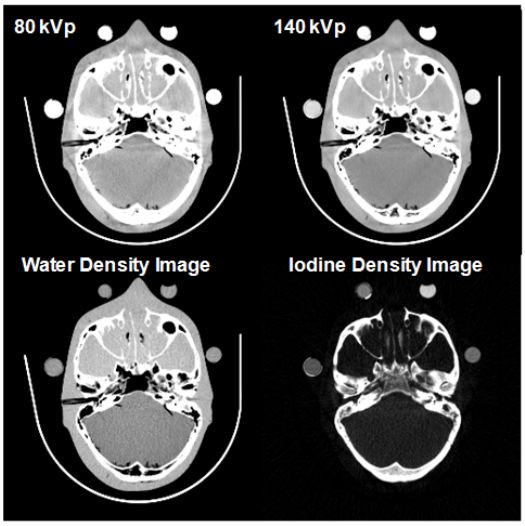

Figure 8: Exemplary reconstructed basis material density images, as well as the kVp images, from a FKS dual-energy head CT exam.

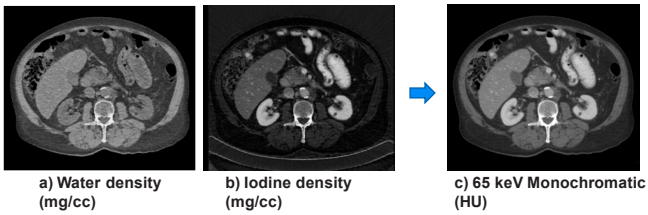

Figure 9: Reconstruction of monochromatic energy image from a pair of basis material density images. The monochromatic energy image, which represents attenuation data that would be measured with a mono-energetic X-ray source at any specific keV level, is computed by combining the basis material density images using Equation 8.

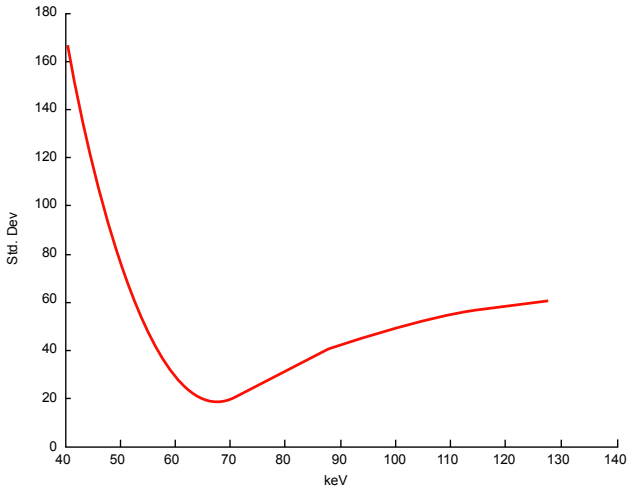

Figure 10: The noise in the generated monochromatic energy images is energy dependent. For FKS dual-energy CT imaging, the noise curve exhibits a global minimum near 65 keV for the particular acquisition protocol. Image adapted from Li et. al, Med. Phys. 38(5), 2595-2601 (2011).

From Equation 8, the expected image noise (variance) in the monochromatic image can be expressed based on linear system theory and noise propagation principle:

$$\delta^2_{mono} = \left[\left(\frac{\mu_1}{\rho_1}\right)(E)\right]^2 \sigma^2_{f_1} + \left[\left(\frac{\mu_2}{\rho_2}\right)(E)\right]^2 \sigma^2_{f_2}. \quad (9)$$

Equation 9 implies that the noise in the generated monochromatic energy image is also energy dependent. This has been confirmed through phantom experiment. Figure 10 plots the measured noise (in HU) as a function of monochromatic energy level, in the range of 40 to 140 keV, for a 20 cm water phantom. The noise curve exhibits a global minimum near 65 keV for the particular acquisition protocol.

Effective atomic number

The X-ray linear attenuation coefficient of a periodic element, μ, can be expressed as a function of the element's material properties and E:

$$\left(\frac{\mu}{\rho}\right)(E) = \sigma(E)\frac{N_A}{A}, \quad (10)$$

where σ, N_A, and A are the total effective cross section, Avogadro's number and the mass number.

The total effective cross section of X-ray radiation in function of the chemical composition of the materials can be modeled as a combination of the Compton and photoelectric effects [23]:

$$\sigma(E) = a(E)Z_{eff} + b(E)Z_{eff}^{C(E)}, \quad (11)$$

where Z_{eff} is the effective atomic number. The coefficients a, b, and c depend only on the energy and their values can be obtained from NIST [24].

By plugging (11) into (10), the linear attenuation can be further expressed as

$$\mu(E) = \left(a(E)Z_{eff} + b(E)Z_{eff}^{C(E)}\right)\frac{N_A\rho}{A}. \quad (12)$$

The simultaneous equations are formed using Equation 12 for two monochromatic energy images $\mu(E_1)$ and $\mu(E_2)$. Solving the simultaneous equations, Z and ρ can be obtained as follows,

$$Z_{eff} = \left[\frac{A}{N_A\rho}\cdot\frac{a(E_2)\mu(E_1) - a(E_1)\mu(E_2)}{a(E_2)b(E_1) - a(E_1)b(E_2)}\right]^{1/C(E)}. \quad (13)$$

Z_{eff} describes the periodic elements most closely representing its energy dependent attenuation behavior, hence it often provides insight regarding the material's chemical composition. Knowledge of the effective atomic number of critical tissue types or specific contrast agents may be leveraged to define and import custom basis materials, allowing for the enhancement of specific anatomical structures.

Figure 11 shows graphically the distribution of several materials commonly encountered in diagnostic radiology in the basis material space (water and bone). Materials are clearly separated based their chemical decomposition. The effective atomic number of each material is reflected by the angular slope. Noise is primarily responsible for the scatter of points in each material and the overlap between different materials.

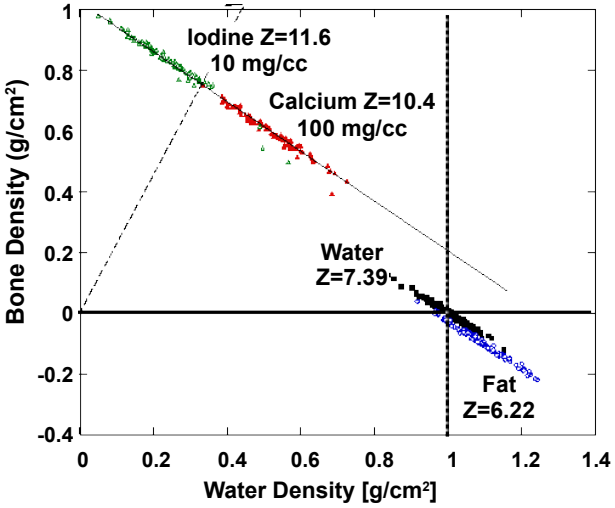

Figure 11: Graphic representation of several materials commonly encountered in diagnostic radiology in the plane of two basis materials (water and bone). Materials are clearly separated based their chemical decomposition. The effective atomic number of each material is reflected by the angular slope. Noise is primarily responsible for the scatter of points in each material and the overlap between different materials.

Noise Suppression

It is well known that the basis material density images have a much lower Signal-to-Noise Ratio (SNR) than single-energy CT images. This can be easily demonstrated by the following simple analysis. Let's define the SNR of Iodine in a low-kVp image as

$$SNR_L(x,y) \propto \frac{\mu_L^I(x,y)}{\sigma_L(x,y)} \tag{14}$$

Then the SNR of Iodine in a basis material density image is

$$SNR_{\Delta E}(x,y) \propto \frac{\mu_L^I(x,y) - R^T \mu_H^I(x,y)}{\sqrt{\sigma_L^2(x,y) + (R^T)^2 \sigma_H^2(x,y)}} . \tag{15}$$

By comparing (15) with (14), and using the fact that μ_L^I and μ_H^I are very close for the most of relevant energy levels, it can be concluded that

$$SNR_{\ E}(x,y) << SNR_L \tag{16}$$

A reduction of noise can be achieved by increased exposure. But based on X-ray physics, a noise reduction by a factor of n requires an exposure increase by a factor of n^2, which leads to unacceptable dose levels for most patients. Therefore, noise suppression has to be automatically applied to FKS dual-energy CT imaging and on the basis material density images in order to enhance the quality of the image while preserving the density values. This allows for a quantitative basis material density image with good image quality.

Noise reduction techniques that attempt to directly reduce noise in basis material density images have also been sought after. To this date, none of them have had success in reducing noise to satisfactory levels while minimally affecting iodine contrast without introducing artifacts.

A more significant improvement in SNR, however, results from the understanding the physical property of the noises that exist in basis material density images. It has been proven that the noises in the two resulting basis material density images are negatively correlated [2,8]. Taking advantage of this property, several noise suppression algorithms have been developed [8,25]. These algorithms subtract a weighted high-pass filtered version of the first basis material density image (e.g., water) to noise reduce the complimentary basis material density image (e.g., iodine).

These algorithms are effective in suppressing noise. However, they are at the risk to introduce a detrimental artifact. Although the high-pass filtered image is smoothed, edge structures and blood vessels full of contrast medium are added to the complimentary basis material density image, causing "cross-contamination" that changes the accuracy of the density values.

The solution, however, exists if the correlated anisotropic diffusion algorithm is employed [26]. The correlated anisotropic diffusion algorithm diffuses both basis material density images (e.g., water and iodine) at the same time. The correlated diffusion strength consists of components corresponding to the image gradients from both images, and the ratios between image gradients. After the diffusion, a noise mask can be computed for each basis material density image as the difference between the original image and its filtered version. Finally, a water (or iodine) noise mask is weighted and then added to the iodine (or water) density image to cancel the correlated noises.

The effectiveness of the correlated anisotropic diffusion algorithm is demonstrated in Figure 12. In this clinical example, the original water and iodine density images are very noisy. Noise reduced water density image using a single-pass algorithm, where the cross-contaminated structures are clearly visible throughout the liver area. By comparing the complimentary noise reduced iodine density image, one can correlate the contaminations in the water density image with the iodinated hepatic vessels in iodine density images. Using the two-pass algorithm, noise reduced water density image is free of contamination.

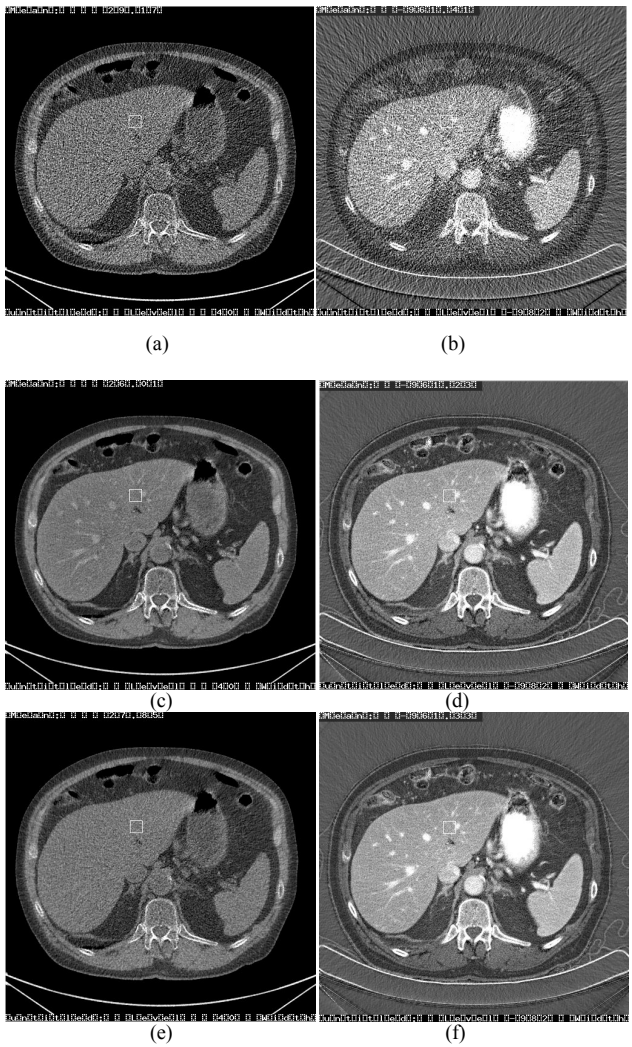

Figure 12: Example of noise suppression of a FKS dual-energy CT imaging using the correlated anisotropic diffusion algorithm. (a) Original water density image. (b) Original iodine density image. (c) Noise reduced water density image using a single-pass algorithm, where the cross-contaminated structures are clearly visible throughout the liver area. (d) Noise reduced iodine density image using a single-pass algorithm. The iodinated hepatic vessels are the root cause of the cross-contaminations seen in the complimentary water image in (c). (e) Noise reduced water density image using the two-pass algorithm is free of contamination. (f) Noise reduced iodine density image using the correlated anisotropic diffusion algorithm. Image adapted from Li et. al, BioMed Research International (2013-in press).

Clinical Applications in Orthopedics

FKS dual-energy CT imaging provides diagnostic information beyond that have been found in conventional single-energy CT imaging, in a manner consistent with workflow, and that increases the efficacy of clinical diagnosis. The clinical application and visualization of dual-energy data is presently an area of active research.

Research into FKS dual-energy CT imaging has been conducted in multiple clinical applications. A discussion of abdominal applications may be found in [15,27]. More recently, attention has been given to apply FKS dual-energy CT imaging to orthopedics applications, due to its excellent temporal-spatial resolution and potential for reduced beam hardening and reduced metal-related artifacts.

One research team compared the extent of metal artifacts between conventional single-energy CT and FKS dual-energy in an animal model with two 5.5 mm diameter stainless steel scoliosis rods inserted into the paraspinal thoracolumbar regions. They found that the monochromatic energy image from FKS dual-energy CT shows noticeable less metal artifacts and significantly better interpretability than single-energy CT ($p<0.05$) [28,29].

In another study, the researchers conducted first a phantom study of size and CT number of titanium and stainless steel plates, then a clinical study involving 26 patients with metallic hardware. They concluded that FKS dual-energy CT imaging can improve the delineation of prosthesis and periprothetic regions which would otherwise be corrupted by artifacts.

The example displayed in Figure 13 demonstrates the increased accuracy in hip implant assessment from FKS dual-energy CT imaging, through improved differentiation of hip bone and metallic implant, enabling accurate measurement of joint spacing.

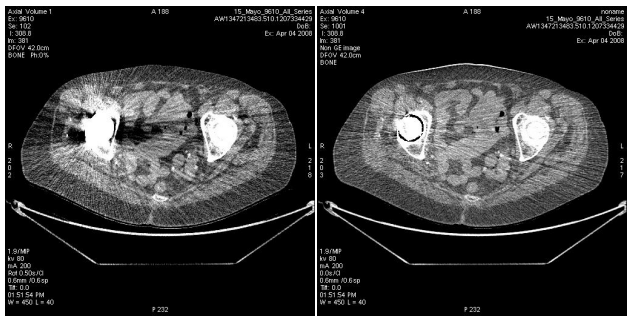

(a) (b)

Figure 13: Example of metal artifact reduction of FKS dual-energy CT imaging. (a) Single-energy CT exam. (b) FKS dual-energy CT exam. Image courtesy of Robert Beckett, GE Healthcare, Waukesha, WI.

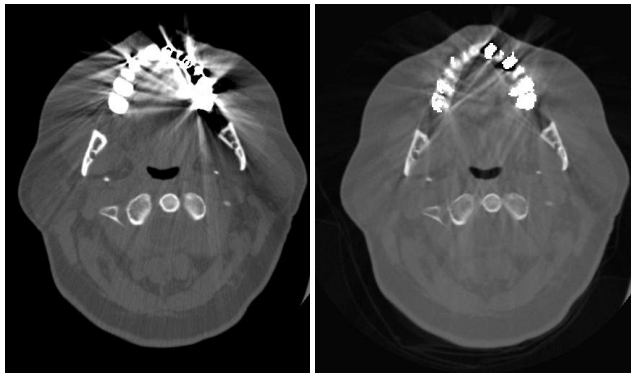

(a) (b)

Figure 14: Example of metal artifact reduction of FKS dual-energy CT imaging. (a) Single-energy CT exam. (b) FKS dual-energy CT exam. Image courtesy of Robert Beckett, GE Healthcare, Waukesha, WI.

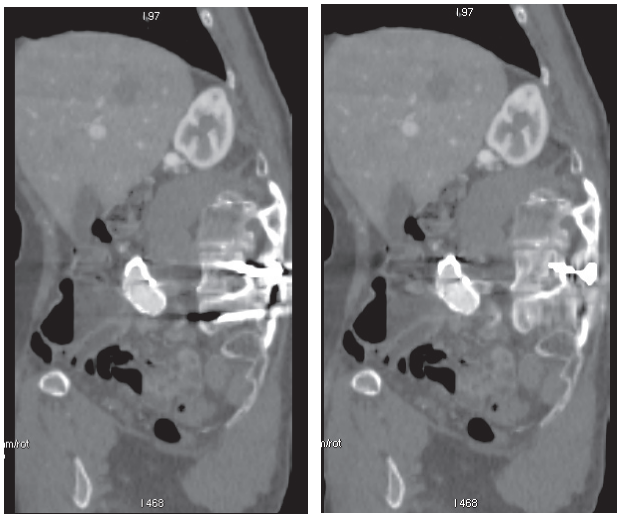

(a) (b)

Figure 15: Example of metal artifact reduction of FKS dual-energy CT imaging. (a) Single-energy CT exam. (b) FKS dual-energy CT exam. Image courtesy of Dr. Amy Hara, Mayo Clinic, Scottsdale, AZ.

Another excellent example of metal artifacts from pedicle screws is shown in sagittal reformatted postoperative spinal CT (Figure 15a). The reconstructed FKS dual-energy CT image (Figure 15b) displays significantly less streak artifacts, enabling much improved visualization of the dural sac and spinal muscles.

Conclusion

Metal artifact reduction still remains a clinical challenge for orthopedics applications. The fundamental root cause is the beam hardening effect due to the polychromatic X-ray beam. Dual-energy CT with fast-kVp switching technique allows synthetic monochromatic energy images to be generated through material decomposition. The monochromatic energy images are inherently free of beam hardening, and thus metal artifacts are remarkably reduced. In addition, Dual-energy CT with fast-kVp switching also provides a broad energy range for optimal contrast at bone-tissue interface. Preliminary clinical studies have demonstrated this new technology's potential in improving image quality and reducing metal artifacts for a broad range of orthopedics applications.

References

1. Alvarez RE, Macovski A (1976) Energy-selective reconstructions in X-ray computerized tomography. Phys Med Biol 21: 733-744.
2. Alvarez R, E Seppi (1979) A comparison of noise and dose in conventional and energy selective computed tomography. IEEE Trans Nucl Sci 26: 2853–2856.
3. Genant HK, Boyd D (1977) Quantitative bone mineral analysis using dual energy computed tomography. Invest Radiol 12: 545-551.
4. Cann CE, Gamsu G, Birnberg FA, Webb WR (1982) Quantification of calcium in solitary pulmonary nodules using single- and dual-energy CT. Radiology 145: 493-496.
5. Coleman AJ, Sinclair M (1985) A beam-hardening correction using dual-energy computed tomography. Phys Med Biol 30: 1251-1256.
6. Kalender WA, Perman WH, Vetter JR, Klotz E (1986) Evaluation of a prototype dual-energy computed tomographic apparatus. I Phantom studies. Med Phys 13: 334-339.
7. Vetter JR, Perman WH, Kalender WA, Mazess RB, Holden JE (1986)

Evaluation of a prototype dual-energy computed tomographic apparatus. II. Determination of vertebral bone mineral content. Med Phys 13: 340-343.

8. Kalender WA, Klotz E, Kostaridou L (1988) An algorithm for noise suppression in dual energy CT material density images. IEEE Trans Med Imaging 7: 218-224.
9. S Sengupta, S Jha, D Walter, Y Du, E Tkaczyk, et al. (2005) Dual energy for material differentiation in coronary arteries using electron-beam CT. Proc of SPIE Med Imag 5745: 1306-1316.
10. Maass C, Baer M, Kachelriess M (2009) Image-based dual energy CT using optimized precorrection functions: a practical new approach of material decomposition in image domain. Med Phys 36: 3818-3829.
11. Altman A, Carmi R (2009) A double-layer detector dual-energy CT– principles, advantages and applications. Med Phys 36: 2750-2750.
12. Hsieh J (2009) Dual-energy CT with fast-kVp switching. Med Phys 36: 2749-2749.
13. Li B, Yadava G, Hsieh J (2011) Quantification of head and body CTDI(VOL) of dual-energy x-ray CT with fast-kVp switching. Med Phys 38: 2595-2601.
14. D Xu, D Langan, X Wu, J Pack, T Benson, et al. (2009) Schmitz Dual energy CT via fast kVp switching spectrum estimation. Proc SPIE Med Imag 7258.
15. Jiang H (2010) GE Healthcare's Gemstone Scintillator Development. Proc of Material Sci. and Tech : 1796-2002.
16. Richard S, Siewerdsen JH (2007) Optimization of dual-energy imaging systems using generalized NEQ and imaging task. Med Phys 34: 127-139.
17. Shkumat N, Siewerdsen J, Dhanantwari A, Williams D, Richard S, et al. (2007) Optimization of image acquisition techniques for dual-energy imaging of the chest. Med Phys 34: 3904-3915.
18. Sabol J, Avinash G, Nicolas F, Claus B, Zhao J, et al. (2001) The development and characterization of a dual-energy subtraction imaging system for chest radiography based on CsI:TI amorphous silicon flat-panel technology. Proc SPIE Med Imag 4320: 399–408.
19. Bushberg J, Seibert J, Leidholdt E Jr., Boone J (2002) The essential physics of medical imaging (2nd Edition), Lippincott Williams & Wilkins.
20. McCollough C, Schmidt B, Liu X, Shuai L, Yu L (2011) Dual-energy algorithms and postprocessing techniques, in Dual Energy CT in Clinical Practice, T.R.C. Johnson et al. (eds.), Springer-Verlag Berlin Heidelberg.
21. Maass C, Baer M, Kachelriess M (2009) Image-based dual energy CT using optimized precorrection functions: a practical new approach of material decomposition in image domain. Med Phys 36: 3818-3829.
22. Jackson D, Hawkes D (1981) X-ray attenuation coefficients of elements and mixture. Phys Rep 70: 169-233.
23. Berger M, Hubbell J (1998) NIST XCOM: photon cross section database, NIST Standard Reference Database 8 (XGAM) NBSIR 87: 3597.
24. McCollough CH, Van Lysel MS, Peppler WW, Mistretta CA (1989) A correlated noise reduction algorithm for dual-energy digital subtraction angiography. Med Phys 16: 873-880.
25. Li B, Li B, Luo J, Tang P, Mao J, et al. (2013) Simultaneous Reduction in Noise and Cross-Contamination Artifacts for Dual-Energy X-Ray CT. Biomed Res Int 2013: 417278.
26. Joshi M, Langan D, Sahani D, Ramesh A, Aluri S, et al. (2010) Fast kV switching dual energy CT effective atomic number accuracy for kidney stone characterization. Proc SPIE Med Imag 7622: 76223.
27. Takrouri H, Alnassar M, Amirabadi A, Moineddin R, Doria A, et al. (2012) Metal Artifact Reduction: The Added Value of Rapid KvP Switching Dual Energy CT in Relation to Single Energy CT in a Piglet Animal Model, RSNA Scientific Assembly and Annual Meeting Program, SSQ15-01.
28. Takrouri H, Alnassar M, Amirabadi A, Moineddin R, Doria A,et al. (2012) "Metal Artifact Reduction in Children: The Added Value of Using Metal Artifact Reduction Software (MARS) for Rapid KvP Switching Dual Energy CT, RSNA Scientific Assembly and Annual Meeting Program, SSQ15-04.
29. Lee YH, Park KK, Song HT, Kim S, Suh JS (2012) Metal artefact reduction in gemstone spectral imaging dual-energy CT with and without metal artefact reduction software. Eur Radiol 22: 1331-1340.